J Mater Sci

Chemical routes to materials

Activating dinitrogen for chemical looping ammonia synthesis: nitridation of manganese

Wrya Mohammadi Aframehr[1] and Peter H. Pfromm[1,*]

[1] *Voiland School of Chemical Engineering and Bioengineering, Washington State University, 1505 Stadium Way, Pullman, WA 99164-6516, USA*

Received: 19 January 2021
Accepted: 1 April 2021

ABSTRACT

The earth-abundant transition metal manganese (Mn) has been shown to be useful to activate dinitrogen at atmospheric pressure and elevated temperature by forming bulk Mn nitrides. Mn nitrides could then be used, for example, for ammonia (NH_3) synthesis in a chemical looping process by contacting nitride with gaseous hydrogen (H_2). Here, we present an investigation of the morphology and local time-dependent composition of micrometer-scale Mn plates during nitridation in dinitrogen (N_2) near atmospheric pressure at 700 °C. The main motivation was to obtain design data for chemical looping synthesis of NH_3 and to add to the somewhat sparse literature on nitridation of Mn. The morphology and elemental compositional variation of the nitrided specimens were studied with scanning electron microscopy (SEM), energy dispersive X-ray spectroscopy (EDX), wide angle X-ray diffraction (WAXD), and mass balances. Three possible nitrogen (N) populations that may govern the Mn nitridation and later NH_3 synthesis are identified. After four hours of nitridation, the N weight gain was found to be 9.4 ± 0.7 kgN to nMn^{-1} for the plates used here, resulting in a nitridation depth of 83 ± 8 μm.

Communicated by Handling Editor: Maude Jimenez.

Address correspondence to E-mail: peter.pfromm@wsu.edu

https://doi.org/10.1007/s10853-021-06079-7

Published online: 23 April 2021

GRAPHICAL ABSTRACT

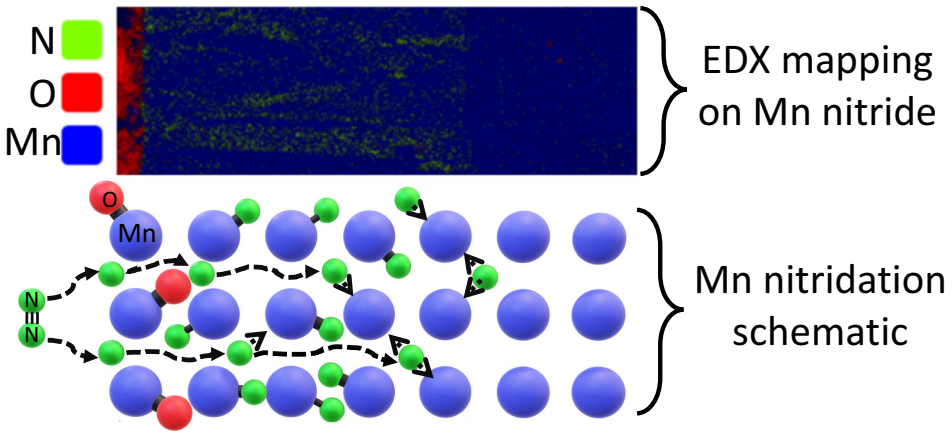

Introduction

Transition metal nitrides are important for semiconductors, improved wear resistance and hardness of materials, magnetic properties, corrosion protection, heterogeneous catalysts, catalytic- and chemical looping NH_3 synthesis, and superconductors [1–7]. The material science literature regarding the Mn nitrides investigated here is not prolific (see summary below), while other transition metal nitrides have attracted more attention. The experimental results presented here may contribute to a more complete view of Mn nitrides.

The novelty of the work presented here resides mainly in the time- and location-dependent tracking of the nitridation process from the surface of a particle into the bulk. Both morphological changes and the presence of N as a function of time and location are the focus. The literature discussion below will reveal that this type of information is currently not readily available.

The motivation for the investigation of metal nitride here is a chemical looping approach to NH_3 synthesis at atmospheric pressure and elevated temperature. NH_3 synthesis has recently attracted attention with a number of approaches proposed in addition to the classical Haber–Bosch process [8–16]. The current interest in NH_3 as an H_2 vector for renewable energy storage and transport is a particular motivation [17], in addition to the synthesis of NH_3 for fertilizers, chemicals, and refrigeration. NH_3 synthesis may benefit from a rugged low pressure process like chemical looping that may scale down to use stranded and intermittent renewable energy on a local or regional scale. Chemical looping for NH_3 synthesis as envisioned here and reported elsewhere [1, 18] consists of converting the bulk of a fixed bed of solid manganese (Mn) particles to Mn nitrides by contacting with N_2 gas at atmospheric pressure and 700 °C. NH_3 is then produced by directing gaseous H_2 over the nitrided Mn, removing N from the bulk nitride. The loop is closed by again nitriding the partially N-depleted Mn. This extends the well-known chemical looping approach [19] where iron (Fe) as an oxygen carrier is cyclically reduced and oxidized [20]. The major difference is that the working metal Mn resides in a solid bed as opposed to the oxygen carrier Fe usually being moved between two reactors [21]. Mn, in particular, is the focus here due to its advantageous balance of the affinity to form nitrides with gaseous N_2 at atmospheric pressure while also allowing NH_3 harvest when subsequently exposed to gaseous H_2 [2, 22].

Mn nitrides have attracted some limited attention, but research regarding the developing morphology and mass transfer of N during nitridation is not readily available. Significant work has been conducted on metal nitrides more recently, aiming to

investigate the nitriding process [23–25]. Iron nitride was one of the first metal nitrides that was thoroughly covered both experimentally and through modeling [26, 27]. Rognerud et al. synthesized Mn_3N_2 via kinetically controlled solid-state metathesis reactions [28]. However, the morphology of the Mn nitride was not studied in detail. Mechanisms of nitriding electrolytic Mn metal were studied by Glück [29]. In this study, the solid-state diffusion into an unreacted shrinking core of metal substrate was developed for the dual-site adsorption of N on the metal surface. The Mn surface activity was the focus, and no detailed information was provided about the nitride layer and events in the bulk [29]. Highly reactive Mn nitride (Mn_3N_2) nanopowders were synthesized by others [30]. The nanoscale of the nitride precluded studies of bulk behavior or morphology. Niewa investigated intermediate phases in the binary system Mn-N and also determined properties of ternary and higher Mn nitrides [31]. Morphology and N mass transfer were not a target of this work. Yang et al. investigated the phase transformation of θ-MnN in thin films to η-Mn_3N_2 using scanning tunneling microscopy [32]. Highly oriented Mn nitride was found. However, diffusion zone growth and the nitride layer morphology were not the focus. Leineweber et al. investigated the nuclear and magnetic properties of the Mn nitride phases (g-Mn_3N_2 and h-Mn_6N_{5+x} ($x \sim 0.26$)) using neutron diffraction [33]. Magnetic phase transitions and crystal structures were the subjects. The phase stability, electronic structure, heat capacity, and thermal expansion of Mn nitrides were studied [31, 33–35], but without emphasizing the nitride layer growth. A study on the kinetics of Mn particle nitridation by Zhang et al. [33] is somewhat convoluted by the impact of oxidation.

In our previous work, Mn nitride phases and the particle surface morphology and composition were studied for several chemical looping cycles to produce NH_3 [1]. X-ray photoelectron spectroscopy (XPS) showed that the surface was composed to a large part of Mn oxide. The highly reproducible performance encouraged the study of N transport into Mn presented here to obtain in-depth design information regarding the prediction of N uptake of Mn. Elsewhere, Michalsky et al. discussed the hydrogenation of Mn nitrides during NH_3 evolution [18, 36]. In another study, Mn nitride was used for NH_3 synthesis by Shan et al. [37] where the molecular-level pathway of the Mn nitride reduction was the focus. Heidlage et al. [38] examined the evolution of Mn nitride phases as a function of time and temperature at atmospheric pressure. The work presented here extends previous studies towards examining the nitridation process as a function of distance from the gas/solid interface, and time.

In summary, it appears that the present study of location- and time-dependent changes during nitridation of bulk Mn samples is a worthwhile addition to the literature, especially regarding the design of chemical looping NH_3 synthesis processes.

In conclusion, the work presented here expands the information available elsewhere on Mn nitrides and adds information on Mn nitride morphology, N mass transport and diffusion, and nitride diffusion zone growth. In the present work, the time and temperature dependencies of Mn nitride layer growth and diffusion zone growth (microstructural development) during nitridation have been investigated using SEM, EDX, mass balance, and WAXD.

Materials and methods

Mn plate-shaped samples were from Alfa Aesar (No. 36215, plate shape, 0.8-12 mm, 99.98wt% pure (metals basis)). SEM and visual images of as-received materials are shown in Fig. 1. For the calculations, it is assumed that impurities are negligible, and the pre-nitridation solid contains Mn only in the bulk, and a small amount of Mn oxide at the surface.

The experimental setup is shown in Fig. 2. A tube furnace (Thermo Scientific Lindberg/Blue M, No. STF54434C) was used. Compressed helium (He, ultra-high purity) and N_2 (ultra-high purity) were supplied by A-L Compressed Gases Inc., Spokane, WA. A digital flow controller (Teledyne Hastings Instruments HFC-D-302B(H), Teledyne Hastings, Hampton, VA,) was used to control gas flow, occasionally verified using a bubble flowmeter (Fig. 2). Alumina combustion boats (Coorstek Inc. No. 65568) were used. Quartz tubes for the tube furnace (inner diameter 45 mm, Technical Glass Products Inc., No. 45X48) were customized via glass blowing by narrowing on the inlet side to attach the gas feed and provided with custom end caps. All gas handling manifolds were constructed from Swagelok stainless steel fittings and tubing (1/8 inch, Swagelok, S. Kent, WA).

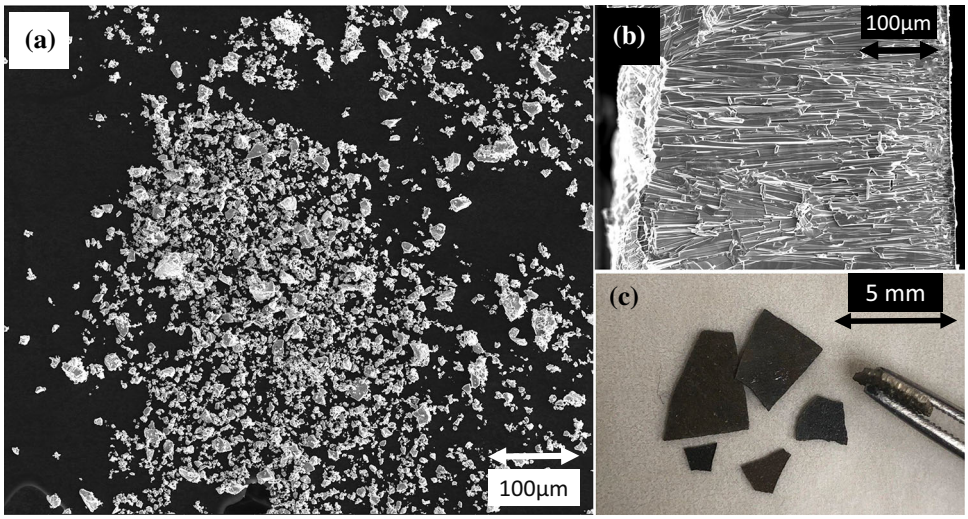

Figure 1 SEM image of Mn powder as-received (**a**). Mn plate SEM and the visual image shown in (**b**) and (**c**), respectively.

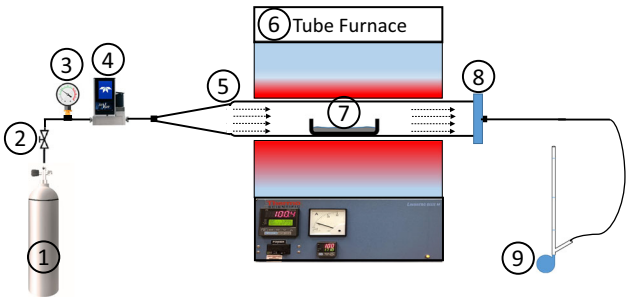

Figure 2 System for chemical looping. (1) N_2 cylinder, (2) metering valve, (3) pressure gauge, (4) digital flow controller, (5) fused quartz tube, (6) electric tube furnace, (7) alumina combustion boat loaded with solid reactant, (8) custom end cap, and (9) bubble flowmeter.

The morphology and qualitative surface composition of Mn powder and Mn plates were examined via an FEI Apreo SEM (FEI Apreo, ThermoFisher Scientific, Waltham, MA, 30 kV, 1 nA).

EDX was used to locate and quantify Mn, N, and O in the samples using an Apreo Volume Scope SEM instrument equipped with a TEAM Pegasus integrated EDX-EBSD (electron backscatter diffraction) system at an accelerating voltage of 20 kV. The low atomic number of N allowed only a comparative evaluation of N content rather than absolute quantification. Mass balance calculations were therefore used to determine absolute N uptake in Mn. Some discontinuities in the EDX line scanning were most likely due to surface roughness. In the EDX line scanning reported below (Fig. 3), the y-axis is X-ray photon detection (count), and the horizontal x-axis indicates the distance (resolution 1 µm = 15points).

EDX scans revealed that the cross-sectional intensity for Mn before and after nitridation was not approximately constant as would be expected since the material is essentially Mn with minor impurities. The data for N after nitridation shown in Fig. 4 were, therefore, normalized according to:

$$I^{\mathrm{nor}}_{\mathrm{Mn,solid}} = I^{\mathrm{raw}}_{\mathrm{Mn,solid}} \times \frac{I^{\mathrm{raw}}_{\mathrm{Mn,nit,av}}}{I^{\mathrm{raw}}_{\mathrm{Mn,solid,av}}} \quad (1)$$

where $I^{\mathrm{nor}}_{\mathrm{Mn,solid}}$ is the normalized intensity for solid Mn in Fig. 4, and $I^{\mathrm{raw}}_{\mathrm{Mn,solid}}$ is the raw intensity data for solid Mn. $I^{\mathrm{raw}}_{\mathrm{Mn,nit,av}}$ and $I^{\mathrm{raw}}_{\mathrm{Mn,solid,av}}$ are the raw data average intensities for solid Mn and Mn after nitridation, respectively.

For nitridation, about 1 g of Mn plate material was loaded into the combustion boat. Samples loaded into the boat were always dried in an oven (Thermo Scientific Lindberg/Blue M, No. VO1218A-1) at 100 °C for about 60 min in ambient air. All processing was at atmospheric pressure. The loaded boat was then placed in the center of the furnace tube. The overall process is shown in Fig. 5. N_2 (1 cm^3 (Standard Temperature and Pressure, STP.) s^{-1}, STP: 1 bar, 0 °C) was directed over the sample at about 100 °C for about 60 min as pre-process drying. The furnace tube was then purged at a gas flow of 1 $cm^3_{(STP)}$ s^{-1} and room temperature for about 10 h before heat up to 700 °C and raising the N_2 flow rate to 2 $cm^3_{(STP)}$ s^{-1}. Cooldown was under 2 $cm^3_{(STP)}$ s^{-1} N_2. After nitridation, weight, SEM (with EDX), and WAXD spectra were obtained.

Performing an experiment identical to nitridation but with He instead of N_2 revealed the maximum

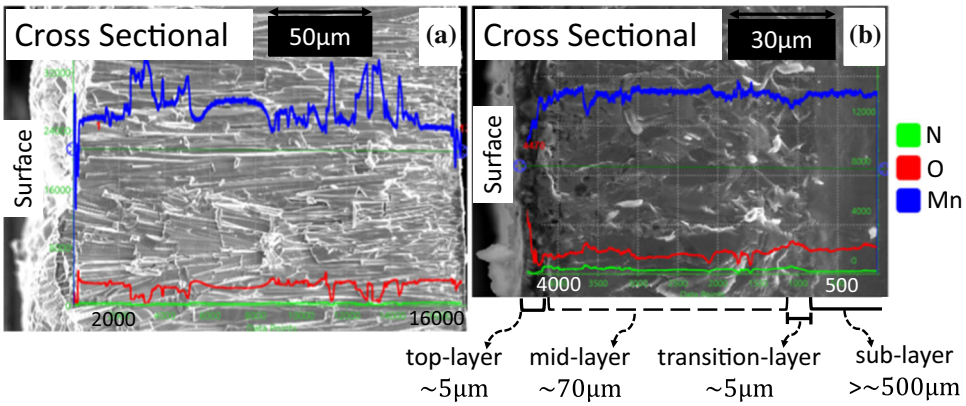

Figure 3 The EDX line spectra of the solid Mn cross-sectional view before (**a**) and after (**b**) 4 h nitridation at 700 °C. Nitridation produces two additional morphologies, coinciding with an increase in N detected (top-to-mid-layer) and a decrease in N detected (mid-layer through transition-layer to unchanged Mn towards the interior of the plates).

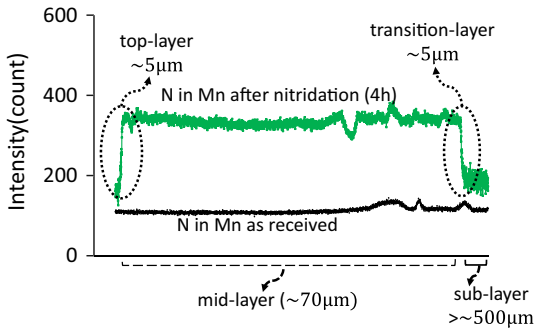

Figure 4 The EDX line spectra of the solid Mn and Mn nitride (4 h nitridation at 700 °C) cross-sectional view. N atom trace shows the increase in N detected (top-to-mid-layer) and a decrease in N detected (mid-layer through transition-layer to unchanged Mn towards the interior of the plate). Raw intensities are re-scaled from Fig. 3 (see, Eq. 1).

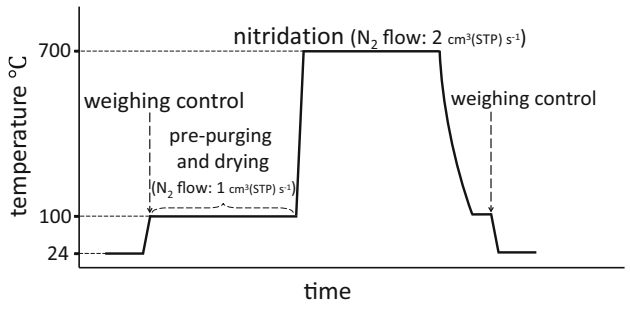

Figure 5 Tube furnace nitridation procedure. Pre-drying and nitrogen pre-purging to sweep air from the reactor was carried out for 1 and ~ 10 h, respectively, at 100 °C and atmospheric pressure, and at 1 $cm^3_{(STP)}\ s^{-1}$ N_2 flow rate. The nitridation was at 700 °C, atmospheric pressure, and 2 $cm^3_{(STP)}\ s^{-1}$ N_2.

content of oxygen uptake due to parasitic oxygen from air (O_2) introduced during nitridation as 0.070 ± 0.007 wt% as calculated from mass balance.

The temperature as set at the furnace controller exceeded the actual temperature in the sample boat by a maximum of 17 °C as determined using a thermocouple (Omega/CL3515R) placed at the alumina combustion boat location (Fig. 2) inside the fused quartz tube. Sample temperatures reported here are the temperatures as set at the furnace controller. Heat up followed the linear relationship in Eq. (2) below while cooling after power off followed Eq. (3) (see Fig. 5).

$$T = 63.86t + 59.03 \quad (2)$$

$$T = 698.58e^{(-0.016t)} \quad (3)$$

where T (°C) and t (min) are furnace controller set-point temperature and time, respectively.

Results and discussion

The time-resolved tracking of N intrusion into Mn and the resulting compositional and morphological changes are discussed below. This is important for the process design of chemical looping to produce NH_3 from Mn nitrides, but it also contributes to basic knowledge on N/Mn interactions, which may be of interest in electrochemistry, metallurgy, and material science.

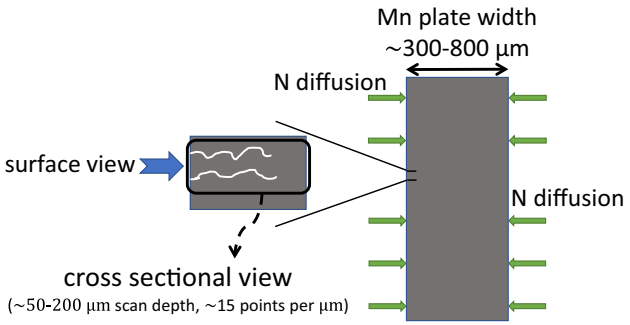

Figure 6 Tracking of N transport into Mn by SEM and EDX analysis of the surface and cross section (after fracture) of an Mn plate after nitridation.

SEM and EDX examination

The experimental tracking of the transport of N atoms into Mn is explored here by exposure of multi-micrometer thickness Mn plates to gaseous N_2 at 700 °C and atmospheric pressure. This allows easy access to the interior after nitridation by simply breaking the plates after cooldown and examining the surface and cross section using SEM and EDX (Fig. 6), assuming that fracturing does not substantially change the N population in the metal matrix. NH_3 synthesis via chemical looping of nitrides will employ not plates but powder with diameters on the multi-micrometer scale or smaller (Fig. 1a). However, the practical difficulties of cross-sectioning such particles after nitridation are circumvented using multi-micrometer thickness plates of the same material.

Figure 7 shows the surface view of an as-received Mn plate. The EDX scanning (Fig. 8) indicates that more than 95 wt% of the surface and the cross-sectional area is Mn as calculated by EDX (EDAX Team Software) analysis. A small amount of oxygen (about 4 wt%) is detected in all EDX scans of as-received Mn, likely due to interaction with atmospheric O_2 prior to scanning.

The increase in oxygen content at the surface of the Mn plate (4 wt% to 20 wt% O over 8 h, Table 1 and Fig. 9) is likely due to some parasitic O_2 introduced with the N_2 gas or minor leaks during the nitridation process. The presence of oxides in the surface of similarly treated Mn samples was confirmed previously via XPS [1].

Two new morphologies appear after nitridation (Figs. 3, 10). These morphologies coincide with changes in N content detected by EDX.

EDX (Table 1) and morphology changes combined with EDX (Fig. 3) indicate a base oxygen content of surfaces exposed to the atmosphere in as-received reference samples. This is likely due to the formation of some Mn oxides. The surface oxygen content increases after nitridation at high temperatures, likely due to further Mn oxide formation.

After nitridation, there is a detectable increase in N content from the oxygen rich top-layer to a roughly constant level in the mid-layer, which we interpret as indicating the formation of Mn nitrides, also based on previous work identifying phases produced in nitridation via WAXD [1]. The presence of N subsides through a transition-layer to the sub-layer to below detection limits likely due to the absence of N transport to depths far away from the dinitrogen/manganese interface. A clear demarcation in morphology and EDX N scan exists between the Mn nitride and the unaltered Mn. Figure 4 confirms that the N concentration through the mid-layer is essentially uniform.

Figure 4 corroborates the clear demarcation of the sub-layer (no nitrogen detected) compared to the mid-layer (some N), where both a morphology changes from sub-layer to mid-layer are apparent, and N mapping in Fig. 11 confirms likely nitride formation. Surface oxygen is also clearly detected.

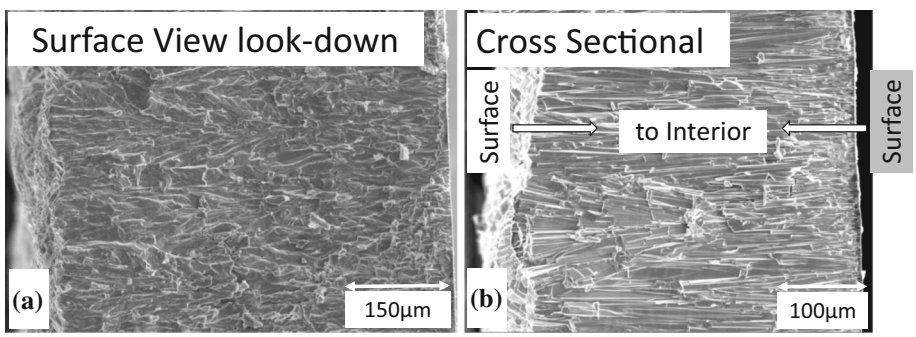

Figure 7 SEM micrograph of an as-received Mn plate: exterior surface look down (**a**) and a cross-sectional view (**b**) after fracturing.

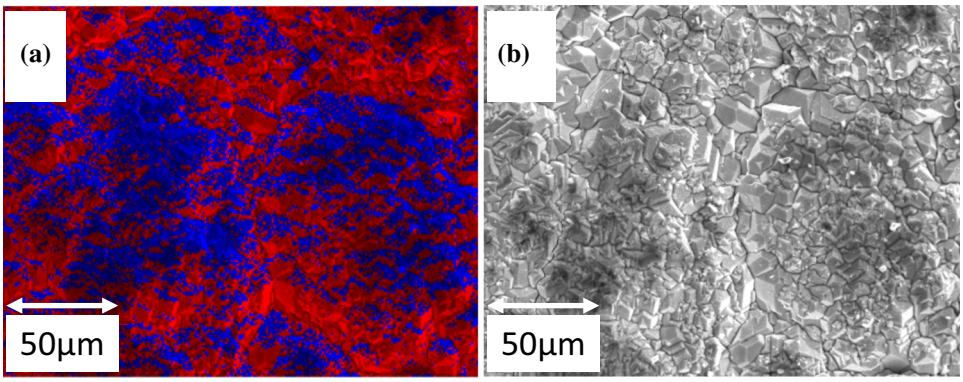

Figure 8 EDX mapping of **a** SEM micrograph, **b** the surface of an as-received Mn plate. Red pixels indicate oxygen, and blue pixels indicate Mn. About 4 wt% oxygen is detected on the surface.

Table 1 The oxygen content (wt%) of the surface and the cross section of Mn plates as-received and after increasing nitridation time

Mn plate	As-received	1 h nitridation	2 h nitridation	4 h nitridation	8 h nitridation
Surface	4 ± 2	8 ± 4	10 ± 4	15 ± 5	20 ± 5
cross section	1 ± 0.5	1.2 ± 0.5	1.2 ± 0.5	1.2 ± 0.5	1.5 ± 0.5

The oxygen content (wt%) of the bulk appears relatively stable, while the oxygen content on the surface clearly increases likely due to parasitic O_2 entering the reactor

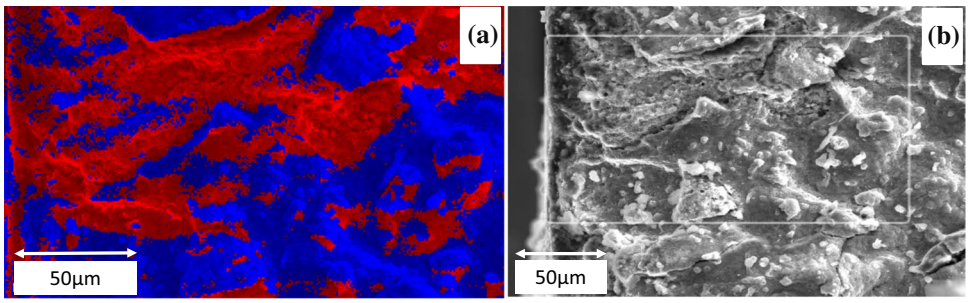

Figure 9 Surface EDX mapping (**a**) and SEM micrograph (**b**) after 4 h nitridation at 700 °C. Red pixels show oxygen, and blue pixels indicate Mn. 15 wt% oxygen is detected on the surface compared to 4 wt% oxygen in as-received Mn surfaces. The additional surface oxygen likely stems from parasitic oxidation during high temperature processing.

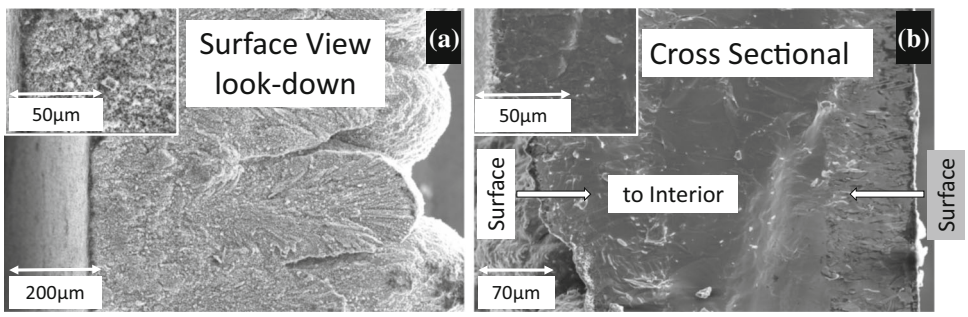

Figure 10 SEM micrograph of Mn **a** surface view (look down), and **b** cross-sectional view after 4 h nitridation at 700 °C. Round structures on the right **b** are the Mn nitride or Mn oxide debris that remained after sample preparation.

Figure 12 shows the progress of nitridation from the surface into the Mn plate bulk with time. The nitridation was tracked via the visible morphology change in SEM combined with the EDX data for Mn content, as discussed above.

Nitrogen transport

General conditions and assumptions

It is assumed that N_2 molecules are split at the metal surface and then migrate as N atoms into the solid.

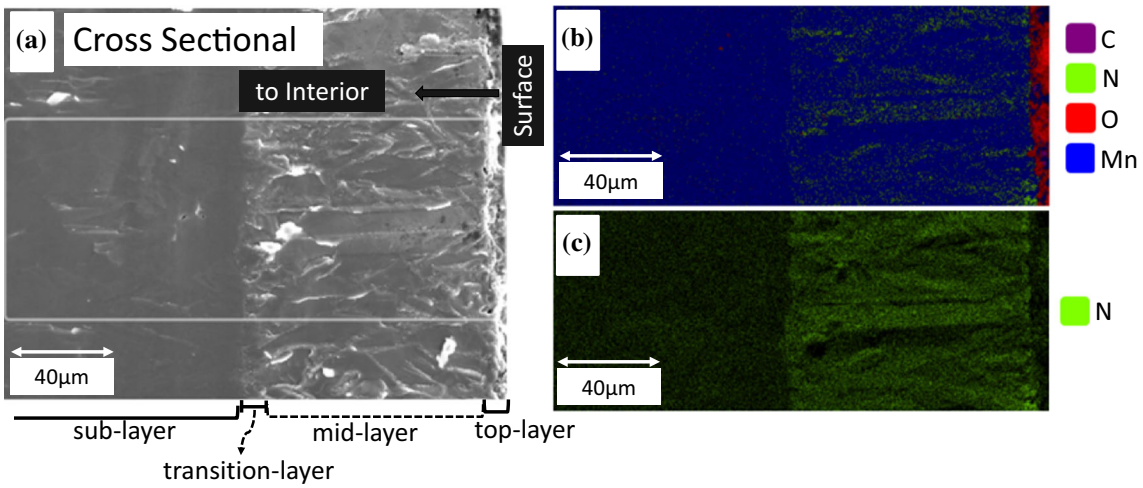

Figure 11 The EDX mapping scan of the Mn nitride with 4 h nitridation at 700 °C. Where **a** is an SEM image of the cross-sectional area shown in **b** as the EDX data shaded for Mn (blue), N (green), and oxygen (red), and in **c** shaded for emphasis of Mn only.

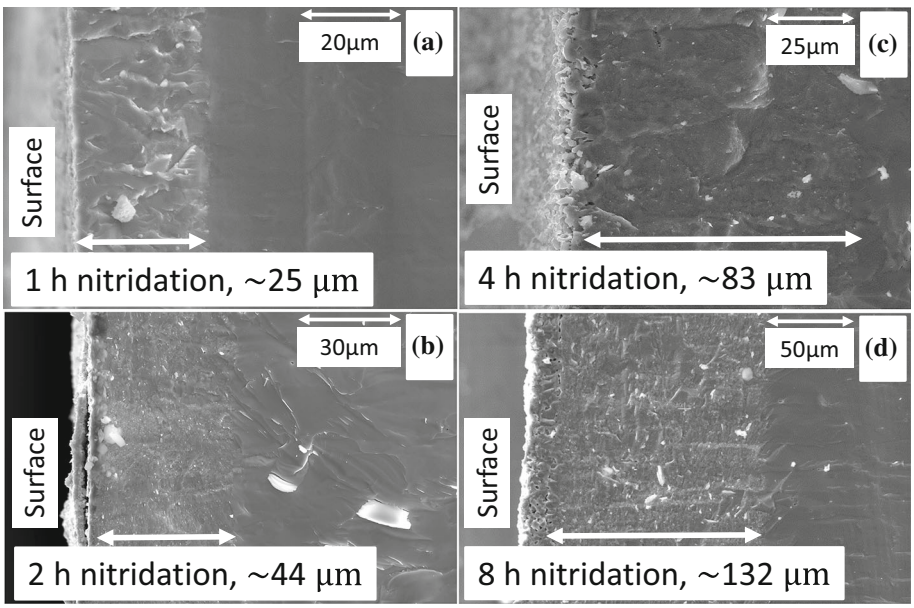

Figure 12 SEM micrograph of the Mn plate cross section **a** after 1 h, **b** 2 h, **c** 4 h, and **d** 8 h nitridation. Increasing nitridation duration results in increasing mid-layer width.

This assumption appears reasonable based on previous work [39, 40].

Figure 12 shows the snapshots of the dynamic process of N atoms penetrating into the solid Mn plate. These snapshots are assumed to represent the situation in the solid at a given time of exposure to gaseous N_2 at 700 °C and atmospheric pressure, then "frozen" by cooling the plate and fracturing it to gain access to the interior for imaging. N_2 splitting and N atom diffusion cease quickly when cooling takes place to below about 500 °C.

Nitrogen populations

Our previous study [1] demonstrated via WAXD that Mn is converted to nitrides when exposed to N_2 at 700 °C and atmospheric pressure as applied here. Three populations of absorbed N in Mn are postulated (see Fig. 13):

> Population 1: atomic N that is strongly bonded (for the definition of 'strong' and 'weak' Me-N interaction, see; [41]) to Mn. Population 1 is not removed by contacting with hydrogen at 700 °C to produce NH_3. This is based on the finding that only about 43 atom % of N is removed from nitrided Mn after

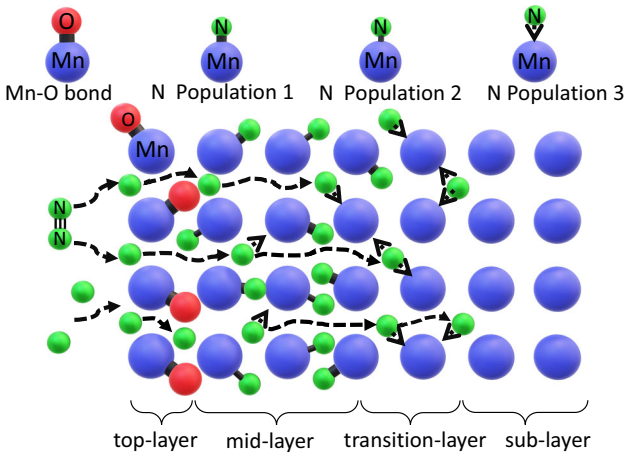

Figure 13 Simplified schematic with Mn oxide near the surface during N transport into the bulk of the Mn. Oxygen is not mobile as MnO. There is a bonded N population 1 (~ 57 atom% of N atoms) and N population 2 (~ 43 atom% N atoms). Furthermore, dissolved N (Population 3), which is quite mobile. Population 1, 2, and 3 are present in the mid-layer, with decreasing concentration in the transition-layer. The sub-layer has not been penetrated by N. Approximate ratios shown are estimated combining mass balances and hydrogenation experiments.

exposure to gaseous H_2 for NH_3 harvesting (20 h, 700 °C).

Population 2: atomic N that is bonded by a covalent/ionic hybrid bond. Consequently, this population can be removed during exposure to H_2 for NH_3 harvesting.

Population 3: N that resides in imperfections of the Mn lattice. This population can diffuse through existing nitride towards the bulk and is converted to nitride once it encounters available metallic Mn.

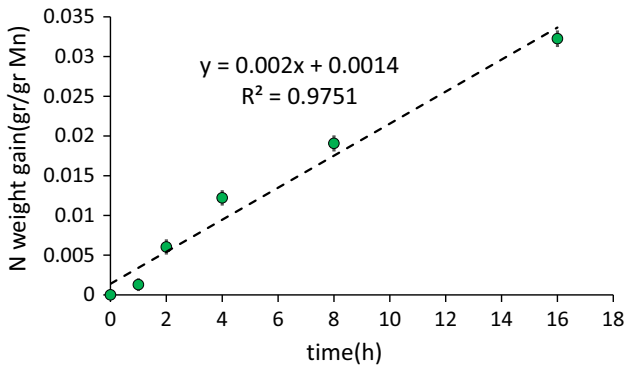

Figure 14 The N weight gain (experimental result) in the nitridation process over time in Mn plate at 700 °C and atmospheric pressure. The line indicates that the experimental result conforms well to a linear fit.

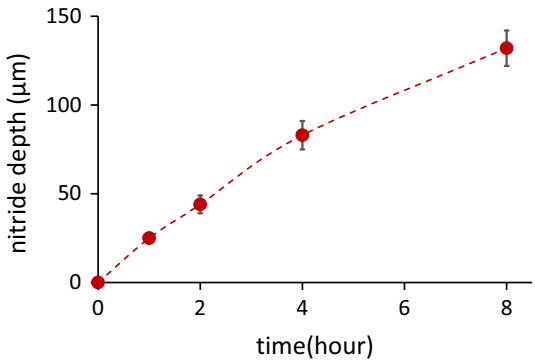

Figure 15 Distance from the surface of the nitrided Mn plate to the intersection of the transition-layer and the sub-layer (see Fig. 12). The dashed line is to guide the eye only.

Scaleup and design

Equation 4 shows the best fit (Fig. 14) to calculate N weight gain in the nitridation process of Mn plates with a size range of 0.8–12 mm in length and width, and 0.3–0.5 mm in thickness (estimated, see Fig. 1b and c), to aid design and scaleup of the nitridation process, and predict nitride amount and depth in solid Mn. For example, based on Figs. 14 and 15, N weight gain is 5.4 ± 0.7 kg ton Mn^{-1} and 17.4 ± 0.8 kg ton Mn^{-1} for 2 and 8 h nitridation at 700 °C and atmospheric pressure, respectively. The

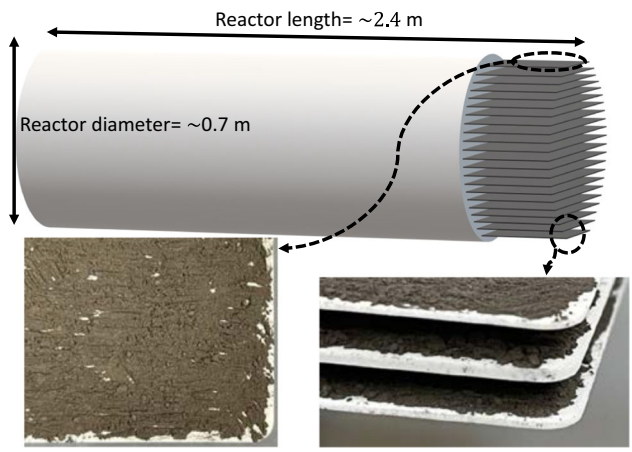

Figure 16 Schematic reactor concept for chemical looping synthesis of NH_3 with Mn distributed on the lamellae of the reactor support. Note: The number of lamellae (thickness 0.55 ± 0.05 mm) inside of the reactor is estimated at 466 and the distance between them is about 1 mm.

depth of the nitridation layer is 44 ± 5 μm and 132 ± 10 μm, respectively.

A best fit for the data in Fig. 14 is

$$W = 0.002t + 0.0014 \quad (4)$$

where W is N weight gain (gr/gr Mn), t is the nitridation time in hours at atmospheric pressure and 700 °C, and ln is the natural logarithm.

Based on the experimental data for harvesting NH_3 from Mn nitride powder (estimated, see Fig. 1a) after 4 h nitridation at 700 °C and atmospheric pressure, and 20 h hydrogenation for NH_3 harvest at 700 °C and atmospheric pressure, 3.52 ± 0.22 $kgNH_3$ $tonMn^{-1}$ day^{-1} can be harvested. A reactor with about 1.68 m^3 volume (see Fig. 16) could be used for NH_3 harvesting at this scale. Other options may be to deposit Mn powder in microchannel reactors or commercial multi-channel ceramic monoliths well known from automotive catalysts. The process can be significantly accelerated by using smaller particles than assumed above.

Conclusions

Morphology changes detected by SEM, along with mass balances, and EDX yielded a coherent picture of nitridation of solid manganese by exposure to gaseous N_2 at atmospheric pressure and 700 °C. The evolution of three distinct morphological regions with time was quantified and reduced to a simple design equation. This equation can be used to estimate material needs for a fixed bed chemical looping reactor to produce NH_3 from gaseous N_2 and H_2 by first nitriding manganese and then contacting manganese nitride with H_2. This NH_3 synthesis approach may be useful for down-scaling or to produce NH_3 in locations where the technically demanding high-pressure Haber–Bosch process may be challenging to implement.

Acknowledgements

This research was supported by the National Science Foundation under Grant No. 1856084 for the FEWtures project. We gratefully acknowledge access to the Franceschi Microscopy and Imaging Center, L.J. Smith Hall, at Washington State University.

Declaration

Conflict of interest The authors declare that they have no conflict of interest.

References

[1] Aframehr WM, Huang C, Pfromm PH (2020) Chemical looping of manganese to synthesize ammonia at atmospheric pressure: sodium as promoter. Chem Eng Technol 43:2126–2133. https://doi.org/10.1002/ceat.202000154

[2] Michalsky R, Pfromm PH (2012) An ionicity rationale to design solid phase metal nitride reactants for solar ammonia production. J Phys Chem C 116:23243–23251. https://doi.org/10.1021/jp307382r

[3] Shalom M, Ressnig D, Yang X et al (2015) Nickel nitride as an efficient electrocatalyst for water splitting. J Mater Chem A 3:8171–8177. https://doi.org/10.1039/c5ta00078e

[4] Sirajuddeen MMS, Banu IBS (2015) Electronic and magnetic properties of Fe(Mn)-doped Cd and Zn nitrides for spintronic applications: a first-principles study. J Mater Sci 50:1446–1456. https://doi.org/10.1007/s10853-014-8705-2

[5] Kumar V, Roy DR (2018) Structure, bonding, stability, electronic, thermodynamic and thermoelectric properties of six different phases of indium nitride. J Mater Sci 53:8302–8313. https://doi.org/10.1007/s10853-018-2176-9

[6] Gharavi MA, Armiento R, Alling B, Eklund P (2020) Theoretical study of the phase transitions and electronic structure of (Zr0.5, Mg0.5)N and (Hf0.5, Mg0.5)N. J Mater Sci. https://doi.org/https://doi.org/10.1007/s10853-020-05372-1

[7] Rudziński M, Zlotnik S, Wójcik M et al (2021) Mask-free three-dimensional epitaxial growth of III-nitrides. J Mater Sci 56:558–569. https://doi.org/10.1007/s10853-020-05187-0

[8] Juangsa FB, Aziz M (2019) Integrated system of thermochemical cycle of ammonia, nitrogen production, and power generation. Int J Hydrogen Energy 44:17525–17534. https://doi.org/10.1016/j.ijhydene.2019.05.110

[9] Edrisi A, Mansoori Z, Dabir B (2014) Using three chemical looping reactors in ammonia production process—a novel plant configuration for a green production. Int J Hydrogen Energy 39:8271–8282. https://doi.org/10.1016/j.ijhydene.2014.03.119

[10] Liu H, Han W, Huo C, Cen Y (2020) Development and application of wüstite-based ammonia synthesis catalysts. Catal Today 355:110–127. https://doi.org/10.1016/j.cattod.2019.10.031

[11] Pfromm PH (2017) Towards sustainable agriculture: fossil-free ammonia. J Renew Sustain Energy 9. https://doi.org/https://doi.org/10.1063/1.4985090

[12] Michalsky R, Parman BJ, Amanor-boadu V, Pfromm PH (2012) Solar thermochemical production of ammonia from water, air and sunlight: thermodynamic and economic analyses. Energy 42:251–260. https://doi.org/10.1016/j.energy.2012.03.062

[13] Heidlage MG, Kezar EA, Snow KC, Pfromm PH (2017) Thermochemical synthesis of ammonia and syngas from natural gas at atmospheric pressure. 14014–14024. https://doi.org/https://doi.org/10.1021/acs.iecr.7b03173

[14] Michalsky R, Pfromm PH (2012) Thermodynamics of metal reactants for ammonia synthesis from steam. Nitrogen Biomass Atmos Pressure 58:3203–3213. https://doi.org/10.1002/aic

[15] Michalsky R, Avram AM, Peterson BA, et al (2015) Chemical science pressure ammonia synthesis for energy storage †. 3965–3974. https://doi.org/https://doi.org/10.1039/c5sc00789e

[16] Chen JG, Crooks RM, Seefeldt LC, et al (2018) nitrogen transformations 6611. https://doi.org/https://doi.org/10.1126/science.aar6611

[17] Aakko-saksa PT, Cook C, Kiviaho J, Repo T (2018) Liquid organic hydrogen carriers for transportation and storing of renewable energy—review and discussion. J Power Sources 396:803–823. https://doi.org/10.1016/j.jpowsour.2018.04.011

[18] Michalsky R, Avram AM, Peterson BA et al (2015) Chemical looping of metal nitride catalysts: low-pressure ammonia synthesis for energy storage. Chem Sci 6:3965–3974. https://doi.org/10.1039/c5sc00789e

[19] Singstock NR, Bartel CJ, Holder AM, Musgrave CB (2020) High-throughput analysis of materials for chemical looping processes. Adv Energy Mater 10:1–11. https://doi.org/10.1002/aenm.202000685

[20] Abad A (2007) The use of iron oxide as oxygen carrier in a chemical-looping reactor. 86:1021–1035. https://doi.org/https://doi.org/10.1016/j.fuel.2006.09.021

[21] Sun R, Yan J, Shen L, Bai H (2020) Performance and mechanism study of LaFeO3 for biomass chemical looping gasification. J Mater Sci 55:11151–11166. https://doi.org/10.1007/s10853-020-04890-2

[22] Michalsky R, Pfromm PH, Steinfeld A (2015) Rational design of metal nitride redox materials for solar-driven ammonia synthesis. Interface Focus 5:1–10. https://doi.org/10.1098/rsfs.2014.0084

[23] Lengauer W, Wiesenberger H, Mayr W et al (1997) Phase stabilities of transition metal carbides and nitrides investigated by reaction diffusion. J Chim Phys Physico-Chimie Biol 94:1020–1025. https://doi.org/10.1051/jcp/1997941020

[24] Kral C, Lengauer W, Rafaja D, Ettmayer P (1998) Critical review on the elastic properties of transition metal carbides, nitrides and carbonitrides. J Alloys Compd 265:215–233. https://doi.org/10.1016/S0925-8388(97)00297-1

[25] Lengauer W, Ettmayer P (1990) Recent advances in the field of transition-metal refractory nitrides. High Temp High Press 22:13–24

[26] Sun Y, Bell T (1997) A numerical model of plasma nitriding of low alloy steels. Mater Sci Eng A 224:33–47. https://doi.org/https://doi.org/10.1016/S0921-5093(96)10561-X

[27] Hägg G (1928) X-ray studies on the 'nitrides' of iron. Nature 121:826–827. https://doi.org/10.1038/121826a0

[28] Rognerud EG, Rom CL, Todd PK et al (2019) Kinetically controlled low-temperature solid-state metathesis of manganese nitride Mn3N2. Chem Mater 31:7248–7254. https://doi.org/10.1021/acs.chemmater.9b01565

[29] Glück T (1994) Mechanisms of nitriding electrolytic manganese metal. Chem Eng J Biochem Eng J 54:167–173. https://doi.org/10.1016/0923-0467(94)00206-1

[30] Buc MM (2016) Convenient synthesis of nanocrystalline powders of phase-pure manganese nitride g-Mn 3 N 2. 8177–8186. https://doi.org/https://doi.org/10.1007/s10853-016-0094-2

[31] Niewa R (2002) Nitridocompounds of manganese: manganese nitrides and nitridomanganates. Zeitschrift fur Krist 217:8–23. https://doi.org/10.1524/zkri.217.1.8.20801

[32] Yang R, Haider MB, Yang H et al (2005) Scanning tunneling microscopy study of the structural phase transformation in manganese nitride: θ-MnN → η-Mn 3 N 2. Appl Phys A Mater Sci Process 81:695–700. https://doi.org/10.1007/s00339-005-3230-4

[33] Leineweber A, Niewa R, Jacobs H, Kockelmann W (2000) The manganese nitrides η-Mn3N2 and θ-Mn6N(5 + x): nuclear and magnetic structures. J Mater Chem 10:2827–2834. https://doi.org/10.1039/b006969h

[34] Song X, Sun Z, Huang Q et al (2011) Adjustable zero thermal expansion in antiperovskite manganese nitride. Adv Mater 23:4690–4694. https://doi.org/10.1002/adma.201102552

[35] García J, Bartolomé J, González D et al (1983) Thermophysical properties of the intermetallic Mn3MN perovskites I. Heat capacity of the manganese nitride Mn4N. J Chem Thermodyn 15:465–473. https://doi.org/10.1016/0021-9614(83)90044-7

[36] Michalsky R, Pfromm P (2019) Thermochemical ammonia and hydrocarbons, U.S. Patent No. 10,315,967. U.S. Patent and Trademark Office, Washington, DC

[37] Shan N, Chikan V, Pfromm P, Liu B (2018) Fe and Ni Dopants Facilitating Ammonia Synthesis on Mn4N and

mechanistic insights from first-principles methods. J Phys Chem C 122:6109–6116. https://doi.org/10.1021/acs.jpcc.7b12569

[38] Heidlage MG, Kezar EA, Snow KC, Pfromm PH (2017) Thermochemical synthesis of ammonia and syngas from natural gas at atmospheric pressure. Ind Eng Chem Res 56:14014–14024. https://doi.org/10.1021/acs.iecr.7b03173

[39] Selg H, Meka SR, Kachel M et al (2013) Nitriding behaviour of maraging steel: experiments and modelling. J Mater Sci 48:4321–4335. https://doi.org/10.1007/s10853-013-7248-2

[40] Verdiere A, Hofer C, De Waele S et al (2017) Precipitation in simultaneously nitrided and aged Mo-containing maraging steel. Mater Charact 131:21–30. https://doi.org/10.1016/j.matchar.2017.06.014

[41] Mittemeijer EJ, Somers MA (2015) Thermochemical surface engineering of steels. Woodhead Publishing